2020

Evaluating thermoelectric properties of BaTiS3 by density functional theory

T. R. Paudel and E. Y. Tsymbal

ACS OMEGA

http://pubs.acs.org/journal/acsodf

Article

Evaluating the Thermoelectric Properties of $BaTiS_3$ by Density Functional Theory

Tula R. Paudel* and Evgeny Y. Tsymbal

Cite This: *ACS Omega* 2020, 5, 12385−12390

Read Online

ACCESS | Metrics & More | Article Recommendations | Supporting Information

ABSTRACT: $BaTiS_3$ is a semiconductor with a small bandgap of ∼0.5 eV and strong transport anisotropy caused primarily by structural anisotropy; it contains well-separated octahedral columns along the [0001] direction and low lattice thermal conductivity, appealing for thermoelectric applications. Here, we evaluate the prospect of $BaTiS_3$ as a thermoelectric material by using the linearized electron and phonon Boltzmann transport theory based on the first-principles density functional band structure calculations. We find sizable values of the key thermoelectric parameters, such as the maximum power factor PF = 928 μW K^{-2} and the maximum figure of merit ZT = 0.48 for an electron-doped sample and PF = 74 μW K^{-2} and ZT = 0.17 for a hole-doped sample at room temperature, and a small doping level of ±0.25e per unit cell. The increase in temperature yields an increase in both the power factor and the figure of merit, reaching large values of PF = 3078 μW K^{-2} and ZT = 0.77 for the electron-doped sample and PF = 650 μW K^{-2} and ZT = 0.62 for the hole-doped sample at 800 K. Our results elucidate the promise of $BaTiS_3$ as a material for the thermoelectric power generator.

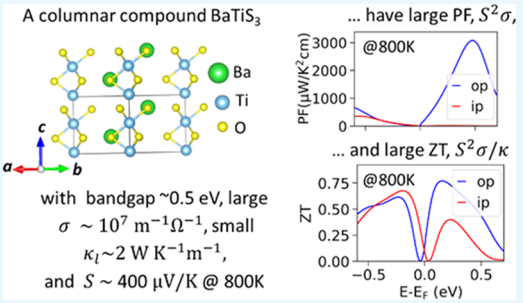

INTRODUCTION

The thermoelectric heat−current conversion process is inefficient compared to other energy conversion technologies such as fossil fuel, solar, and nuclear because of the small thermoelectric figure of merit, ZT, of the materials involved. While a large ZT value of ∼3 to 4 is required for thermoelectric technology to be viable, even optimized thermoelectric bulk materials, including doped SnTe and PbTe,[1−4] have ZT values not exceeding about 2.6, which limits the usage of thermoelectricity in practice as a primary energy source. Alternatively, thermoelectric power generation can supplement the other energy technologies by converting wasted heat into current, thereby increasing the overall efficiency of the system. These thermoelectric power-generating devices are very reliable energy producers as they are free of lifetime-reducing moving parts (the typical lifetime of a thermoelectric device is ∼10^6 h) and serve as a component of a global energy solution system.

The thermoelectric figure of merit, ZT = $(S^2\sigma/\kappa)T$, is a key measure of a material's thermoelectric performance at temperature T, where S, σ, and κ represent the thermoelectric power, electrical conductivity, and thermal conductivity, respectively. The latter is given by the sum of electronic thermal conductivity, κ_e, and lattice thermal conductivity, κ_l. The thermoelectric performance of a material can be enhanced by increasing ZT, which can be achieved by maximizing the power factor, PF = $S^2\sigma$, and minimizing κ.[5] Unfortunately, maximizing PF, for instance, by band engineering,[6] often also increases κ_e, even though the contrary has been reported[7] a significant part of κ, as it is connected to σ by the Wiedemann−Franz law, $\kappa_e\sigma = LT$, where L is a constant equal to 2.44 × 10^{-8} V^2 K^{-2} for a free-electron gas. Fortunately, κ_l can be minimized somewhat independently without interfering with the process of power factor $S^2\sigma$ maximization, thereby optimizing the overall ZT. κ_l can be reduced by using a low-dimensional form of materials, including interfaces, nanostructures, grain boundaries, and amorphous powder, in which the lattice coherency can be tuned, and in the ideal case made smaller than the heat-carrying-phonon mean free path, thereby increasing the phonon scattering.

RESULTS AND DISCUSSION

$BaTiS_3$ is a unique compound of the II-IV-S_3 material class that crystallizes in the hexagonal $P6_3mc$ phase (space group 186, Figure 1a), while other members of this class, such as Ba(Zr,Hf)S_3 and Ba(Zr,Hf)S_3, crystallize in the orthorhombic $Pnma$ phase. $BaTiS_3$ contains one-dimensional edge-sharing octahedral pillars, running along the [0001] directions,[8] that are connected by the van der Waals interaction along the [1000] and [0100] directions. This very anisotropic structure gives rise to giant optical anisotropy, broadband birefringence

Received: March 14, 2020
Accepted: May 14, 2020
Published: May 22, 2020

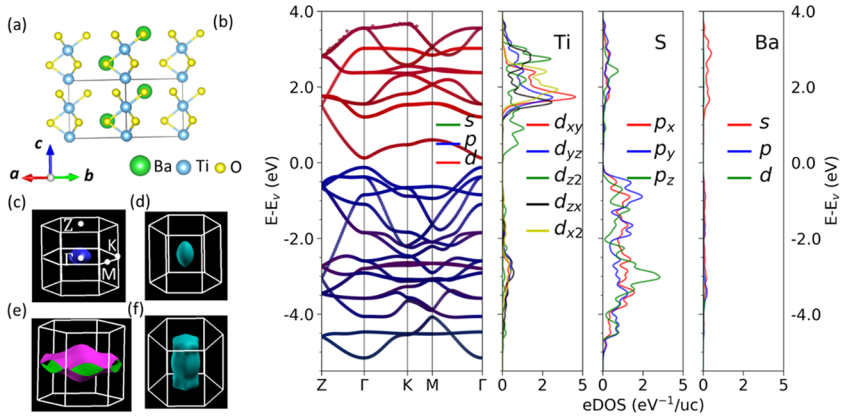

Figure 1. Atomic and electronic structures of bulk $BaTiS_3$. Atomic structure (a), electronic band structure (left panel) and atom- and orbital-resolved density of states (right panels) (b). High symmetry points Γ, *Z*, *K*, and *M* are marked in the Brillouin zone shown in (c). Fermi surface of hole-doped $BaTiS_3$ with concentrations of 0.05 e/uc (c) and 0.5 e/uc (e) and that of electron-doped $BaTiS_3$ with concentrations of 0.05 e/uc (d) and 0.5 e/uc (f).

and dichroism,[9] and ultralow thermal conductivity.[10] The electronic band structure and electronic density of states (eDOS) show that the top of the valence band contains two-fold degenerate in-plane sulfur p_x and p_y bands (Figure 1b). The bottom of the conduction band contains nondegenerate titanium d_{z^2} bands. The spin−orbit coupling does not affect the conduction band, as $l_z = 0$ for the d_{z^2} band, and is very small for the valence band, as it is primarily composed of low-atomic-number s−p-like states. The Fermi surface of the doped $BaTiS_3$ (±0.05 e/uc) represents a Γ-point-centered Fermi ellipse with the major axis pointing along the out-of-plane direction for an electron-doped sample (Figure 1d) and along the in-plane direction for a hole-doped sample (Figure 1c). Upon increasing the doping level to 0.5 e/uc, while the Fermi surface of the hole-doped sample extends in the plane of the Brillouin zone with multivalley degeneracy at the *K* and *K*′ points (Figure 1e), which leads to large DOS and *S*, the Fermi surface of the electron-doped sample extends along the Γ−*Z* direction (Figure 1f), suggesting a low-dimensional nature of the band structure and possibly large σ.

The effective mass of the undoped $BaTiS_3$ (calculated using the band curvature $1/m^* = 1/\hbar^2(\partial^2E/\partial k^2)$) shows that the smallest electron mass is $0.7m_0$ along the out-of-plane direction and the smallest hole mass is $0.8m_0$ along the in-plane direction, where m_0 is a free-electron mass (Table 1). The

Table 1. Calculated Deformation Potentials (E_1) of Valence and Conduction Bands, Elastic Constants, Effective Mass, and Carrier Relaxation Time

type	E_1 (eV)	C_{ip}, C_{op} (Pa)	m^* (m_0)	μ (cm^2 V^{-1} S^{-1})	τ (ps)
e (ip)	7.8	942	1.6	29	0.03
h (ip)	−11.2	942	0.8	80	0.04
e (op)	−3.9	1266	0.7	1240	0.49
h (op)	5.6	1266	1.5	90	0.07

small effective mass indicates the possibility of high mobility. Indeed, the mobility calculated using a single-band deformation model[11] shows a very large value of 1240 V cm^{-1} S^{-1}, similar to TiS_3,[1212] for electron conduction and 90 V/(cm S) for hole conduction. Large mobility suggests high electrical conductivity, $\sigma = ne\mu$, and a long carrier lifetime, $\mu = e\tau/m^*$, for electron conduction.

Based on the large eDOS in the hole-doped sample and large μ in the electron-doped sample, PF is expected to be significant for both electron and hole doping. A combination of large PF and low κ_L suggests that $BaTiS_3$ could be an excellent material for thermoelectric applications. To test this expectation, we explicitly compute σ/τ, *S*, and κ_e/τ using the linearized electron Boltzmann transport theory based on the first-principles density functional band structure calculations assuming constant relaxation time, and κ_l using the corresponding phonon counterparts assuming relaxation time based on three-phonon interactions.[13]

Figure 2a−c shows total eDOS, doping level, *n*, and out-of-plane and in-plane components of σ, *S*, and κ_e/τ as a function

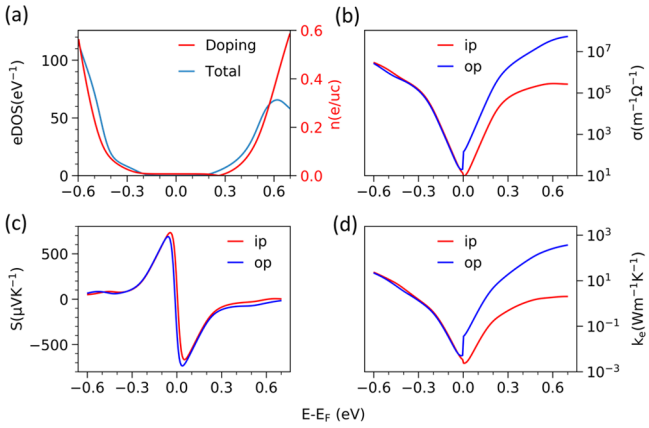

Figure 2. Calculated total electronic density of states eDOS (blue line) and doping concentration *n* (red line) (a), in-plane, ip (red color), and out-of-plane, op (blue color), components of transport coefficients: electronic conductivities σ (b), Seebeck coefficients, *S* (c), and electronic part of thermal conductivities, κ_e (d), at room temperature plotted as a function of the chemical potentials, $\mu_c = E - E_F$.

of the chemical potential, $\mu_c = E - E_F$. The chemical potentials we choose lie within the reasonable doping level of ±0.65 e/uc. As expected for a semiconductor, the eDOS, the doping *n*, and the conductivities, σ and κ, are zero at the Fermi energy; they, however, increase quickly with the increasing μ_c, which can be brought about by doping with electrons or holes, as shown in Figure 2a (red curve). The temperature additionally increases

https://dx.doi.org/10.1021/acsomega.0c01139
ACS Omega 2020, 5, 12385−12390

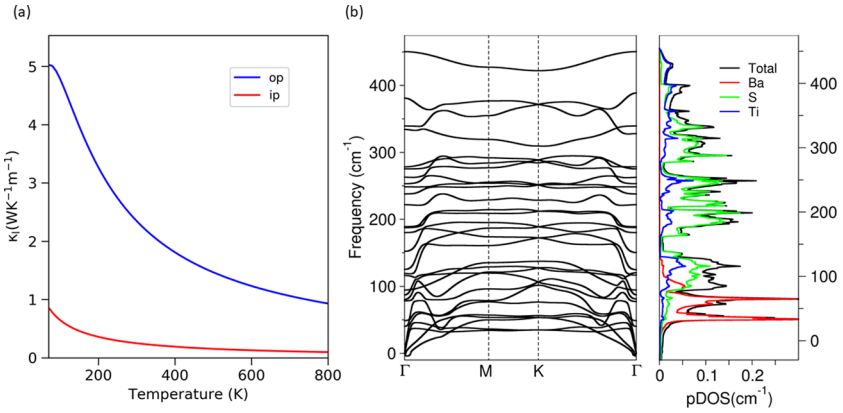

Figure 3. In-plane, ip (red color), and out-of-plane, op (blue color), components of the lattice thermal conductivity, κ_l, as a function of temperature (a) and a phonon band structure and atom-resolved phonon density of states, pDOS (b), as a function of wavenumber.

the conductivity, both electronic and thermal (as can be seen by comparing Figure 2 to Figure S2), typical for a semiconductor. While the conductivity of the hole-doped sample remains mostly isotropic, the conductivity of the electron-doped sample is very anisotropic: the out-of-plane conductivity increases dramatically compared to the in-plane conductivity due to contribution from very dispersive out-of-plane Ti-d_{z^2} bands. Upon increasing the electron doping level beyond 0.65 e/uc, the out-of-plane d_{xz} and d_{yz} bands contribute first to the conductivity (Figure 1b), and eventually, the in-plane bands, $d_{x^2-y^2}$ and d_{xy}, start to participate and the conductivity increases up to 2100 mΩ^{-1} cm^{-1} (1 Ω^{-1} m^{-1} = 10^{-5} mΩ^{-1} cm^{-1}, not shown in the plot). The in-plane component, however, remains small (~1−15 mΩ^{-1} cm^{-1}), giving rise to a very large conduction anisotropy, $\sigma_{op}^{max}/\sigma_{ip}^{max}$, of 225, consistent with the experimental observations.[9]

The Seebeck coefficient, S (also called thermopower), which is proportional to the logarithmic derivative of conductivity with energy, shows a usual sign change at $\mu_c = 0$ with a positive value for hole doping and a negative value for electron doping. For the electron doping, the thermopower has a maximum value of ~735 μV K^{-1} for the out-of-plane component and ~666 μV K^{-1} for the in-plane component. Similarly, for the hole doping, thermopower has a maximum value of ~689 μV K^{-1} for the out-of-plane component and 733 μV K^{-1} for the in-plane component at room temperature. These values are much larger than 150−250 μV K^{-1} associated with good bulk thermoelectric materials.[14] When the temperature is increased, S decreases; however, it remains relatively high, with maximum values of 390 μV K^{-1} for a hole-doped system and 381 μV K^{-1} for an electron-doped system at 800 K (Figure S2), around which temperature of the compound is reported losing S and doping the system n-type.[15] At higher temperature, typically, the most significant peak of S shifts to a higher doping level. However, here it is achieved at a low doping level, ~0.01 e/uc, which is much lower than that in its oxide counterpart, electron-doped $SrTiO_3$.[16]

Figure 3a shows the calculated in-plane and out-of-plane κ_l plotted as a function of temperature. It can be seen that κ_l is also anisotropic (Figure 3a), similar to σ (Figure 2b), with the out-of-plane component of 2.35 V m^{-1} K^{-1} and the in-plane component of 0.25 V m^{-1} K^{-1} at 300 K. The value of κ_l is larger, comparable, and smaller than the electronic thermal conductivity, κ_e, for intrinsic, low-doped, and heavily doped samples, respectively (compare Figure 3a to Figure 2d). Thus, the control of κ_l is crucial for the ZT of intrinsic and low-doped semiconductors. Even the largest values of the calculated κ_l for $BaTiS_3$ are smaller than those reported for the other two-dimensional (2D) materials such as phosphorene, MoS_2, and graphene but comparable to stannate and n-doped STO.[17]

The efficiency of a thermoelectric generator is related to the power factor, PF = $S^2\sigma$. Figure 4a shows PF plotted as a function of μ_c, which is also strongly anisotropic, similar to S and σ. At room temperature, the maximum power factor is 928 μW K^{-2} cm for an electron-doped sample and 74 μW K^{-2} cm for the hole-doped sample. With increasing temperature, the power factor increases and reaches a value of 3078 μW K^{-2} cm for the electron-doped sample and 650 μW K^{-2} cm for the hole-doped sample at 800 K (Figure S3), which is largely contributed by the enlarged σ at the higher temperature (compare Figure 2b to Figure S2b).

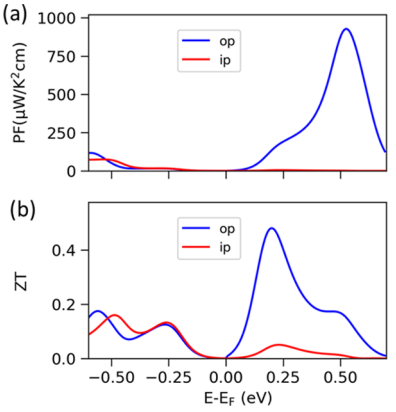

Figure 4. In-plane, ip (red color), and out-of-plane, op (blue color), components of the calculated power factor, PF (a), and thermoelectric figure of merit, ZT (b), at room temperature as a function of the chemical potential, $\mu_c = E - E_F$.

The reason for the small value of κ_l can be gleaned from the computed phonon spectra. Figure 3b shows the computed phonon band structure and phonon density of states (pDOS), and Table 2 shows the frequency of the phonons at the center of the Brillouin zone, which are categorized according to their symmetries within the underlying point group C_{6v}. We see from the phonon spectra that the optical phonons are soft, and there is no gap between the acoustic and optical phonons. There are several reasons for this, including a weak ionic

https://dx.doi.org/10.1021/acsomega.0c01139
ACS Omega 2020, 5, 12385−12390

Table 2. Calculated Born Effective Charge Tensor Components; S_2 Ion is Closer to Ba than S_1

	xx	*yy*	*zz*
Ba	3.4	3.4	3.0
Ti	2.4	2.4	6.7
S_1	−1.2	−2.7	−3.2
S_2	−2.3	−1.6	−3.2

bonding, as evidenced by the large Born effective charges (Table 3) compared to the nominal valence charges, relatively

Table 3. Calculated Dielectric Permittivity Tensor Components

ε	*xx*	*yy*	*zz*
electronic	10	10	13
ionic	19	19	92
total	29	29	105

large ionic screening, as follows from the large values of the dielectric permittivity tensor components (Table 4), and weak

Table 4. Calculated Phonon Modes (cm^{-1}) at the Center of the Brillouin Zone Labeled According to the Symmetry of Irreducible Representations[a]

A_1 (I + R)	A_2	B_1	B_2	E_1 (I + R)	E_2 (R)
18	0	36	78	55	65
235		269		149	120
336		280		200	180
		437		351	241
					260

[a]E_2 mode is Raman active, A_1 and E_1 are both Raman and infrared active, while A_2 and B_2 modes are silent.

interatomic force constants. The nondispersive phonons at the Brillouin zone edges (M and K points) dominate pDOS, which allow for the larger number of phonon interactions responsible for the reduced lattice thermal conductivity. The anisotropy of the lattice thermal conductivity can be qualitatively explained in terms of the anisotropic bonding in the compound. While there is a bonding between Ti and S atoms along the out-of-plane directions, leading to relatively dispersive phonon bands (not shown) with smaller mass, larger velocity, and larger conductivity, the absence of bonding along the in-plane direction leads to the opposite: flatter phonon bands (Figure 3a) with larger mass, smaller velocity, and smaller conductivity.

The better performance measure of thermoelectric materials is a figure of merit, ZT. Figure 4b shows ZT as a function of the chemical potential μ_c at 300 K, which is calculated assuming κ_l is independent of μ_c. For the electron doping, the ZT has a maximum value of 0.48 for the out-of-plane component and 0.05 for the in-plane component. Similarly, for the hole doping, ZT has a maximum value of 0.17 for the out-of-plane component and 0.16 for the in-plane component. ZT increases with the temperature because of the increase in the power factor close to μ_c = 0. For example, for the electron doping, ZT reaches the maximum value of 0.77 for the out-of-plane component and 0.4 for the in-plane component, and for the hole doping, it reaches a maximum value of 0.61 for the out-of-plane component and 0.67 for the in-plane component at 800 K (Figure S3).

The doping level that is required for the maximum value of ZT (0.77) is small and can be easily achieved by doping. For example, *S* vacancies or doping by La (similar to the case of well-known $La_xBa_{1-x}MnO_3$) can make the compound n-type with a good thermoelectric figure of merit. P-doping can be induced by high-temperature growth at a reduced pressure of Ba. The predicted large thermoelectric efficiency of $BaTiS_3$ for both electron- and hole-type conduction is due to the relatively low bandgap and possibly low ionization potentials compared to oxides. Further tuning of the band structure and thermal conductivity is possible by phase intermixing and exfoliations. We find that the alternative centrosymmetric $P6_3mmc$ (space group 194) phase is unfavorable just by $\Delta E \sim 1$ meV fu^{-1}, indicating a possibility for intermixed phases. The calculated cleavage energy of 1.1 J m^{-2} for exfoliation of the compound along the [0001] direction, which is just about three times the corresponding values for MoS_2 and graphene, indicates the possibility of creating low-dimensional ternary chalcogenides.

COMPUTATIONAL METHODS

We used the first-principles density functional theory calculations based on the projected augmented wave method[18] and the Perdew−Burke−Ernzerhof functional,[19] as implemented in the Vienna ab initio simulation package (VASP).[20,21] We fully relaxed the structure, the $P6_3mc$ (space group 186) phase of $BaTiS_3$ (Figure 1a), with the force convergence limit of 0.005 eV/atom. We treated the correlation effects beyond generalized gradient approximation (GGA) at a semiempirical GGA + *U* level within a rotationally invariant formalism[22] with U = 6 eV for the Ti 3d orbitals. The crystal structure was optimized, resulting in lattice parameters $a = b$ = 6.73 Å and c = 5.92 Å, which are very close to the experimental lattice parameters $a = b$ = 6.75 Å and c = 5.8 Å.[8] For the accurate description of the interlayer separation, van der Waal's interaction was included in the calculations.[23]

Phonon band structure was calculated using the density functional perturbation theory, as implemented in the PHonon package of Quantum ESPRESSO. We used 6 × 6 × 6 Monkhorst k-grid to calculate the dynamical matrix. The interatomic force constant in real space was then calculated by Fourier transforming the dynamical matrix calculated in a uniform grid. The phonons at any other *q*-points were then calculated by redoing the Fourier transformation. For the electronic density of states, we used a 12 × 12 × 10 Monkhorst *k*-point mesh.

The conductivities, σ and κ_e, and the Seebeck coefficient, *S*, were calculated using the BOLTZTRAP code,[24] which assumes a constant carrier relaxation time, τ, and can directly calculate the power factor PF = $S^2\sigma$.

We estimated the carrier relaxation time, τ, by single-band approximation using

$$\tau_{ij}(T) = \frac{\mu m^*}{e} = \frac{m^*}{e}\frac{e\hbar^3 C_{ij}}{3K_B T|m^*|^2 E_i^2}$$

where C_{ij}'s are the elastic modulus, m^* is the effective mass, $m_i^* = \hbar^2(\partial^2 E/\partial k_i^2)^{-1}$, $\hbar$ is Planck's constant, k_i is the magnitude of the wave vector in the *i*-direction, T is the temperature, and E_i is the deformation potential. E_i is proportional to the band edge (conduction band minimum (CBM) and valence band maximum (VBM)) shifts, ΔE, induced by lattice dilation, $\Delta l_i/l_i$, along the crystallographic direction, *i*, as $\Delta E = E_i(\Delta l_i/l_i)$. While C_{ij}'s were calculated using

https://dx.doi.org/10.1021/acsomega.0c01139
ACS Omega 2020, 5, 12385−12390

the density functional perturbation theory,[25] E_i's were determined by performing a series of calculations by straining a lattice along the in-plane and out-of-plane crystallographic directions.

The lattice thermal conductivity, κ_l, was calculated from the solution of the linearized phonon Boltzmann equation,[26] assuming its proportionality with the phonon lifetime, which is determined by first-principles anharmonic lattice dynamics[13] using the Phono3py code. The force constants used in the code were computed using VASP with a 2 × 2 × 2 supercell and 6 × 6 × 6 k-points.

Phonon Symmetry. The phonons at the Γ point can be written as $\Gamma = 4A_1 \oplus A_2 \oplus 4B_1 \oplus B_2 \oplus 10E_1 \oplus 10E_2$, where numeric symbols correspond to the phonon count. Out of 30 modes corresponding to 10 atoms in a unit cell, three modes are acoustic type and contain a degenerate E_1 (Figure S1c) mode corresponding to the vibration of the lattice along two in-plane lattice vectors' direction and a nondegenerate A_1 (Figure S1a) corresponding to the vibration of the lattice along the out-of-plane lattice vector direction. The remaining modes are optical. The lowest transverse optical mode has an A_2 (Figure S1b) symmetry and includes an in-plane rotation of S atoms around Ba. This mode is even with respect to all C_6, C_3, and C_2 rotations, but odd with respect to σ_v (contains the main rotation axis) and σ_d reflections (does not contain rotation, still vertical) and silent with respect to both infrared and Raman spectroscopy. Out of the rest, the A_1 mode, symmetric with respect to all symmetry operations of the group, and the E_1 mode, symmetric with respect to C_6 but antisymmetric with respect to C_2 and C_3, are Raman and infrared active. The E_2 mode (Figure S1d), antisymmetric with respect to C_6 and C_3 but symmetric with respect to C_2, is only Raman active. The B_1 mode (Figure S1e), symmetric with respect to C_3 and σ_v but antisymmetric with respect to C_6, C_2, and σ_d, and the B_2 mode (Figure S1f), symmetric with respect to C_3 and σ_v but antisymmetric with respect to C_6, C_2, and σ_d, are both Raman as well as infrared inactive similar to A_2.

■ ASSOCIATED CONTENT

Supporting Information

The Supporting Information is available free of charge at https://pubs.acs.org/doi/10.1021/acsomega.0c01139.

Figure S1: Symmetry-resolved phonon modes. Figures S2 and S3: calculated total electronic density of states, doping concentration, in-plane and out-of-plane components of electronic conductivities, Seebeck coefficients, electronic part of thermal conductivities, power factor, and thermoelectric figure of merit at 800 K plotted as a function of the chemical potentials. Figures S4 and S5: the temperature dependence of the density of states, in-plane and out-of-plane components of electrical conductivity, Seebeck Coefficient, electronic part of thermal conductivity, power factor, and thermoelectric figure of merit plotted as a function of the chemical potentials. Table S1: computational cell parameters and atomic positions, a part Quantum Espresso input file (PDF)

■ AUTHOR INFORMATION

Corresponding Author

Tula R. Paudel − *Department of Physics and Astronomy & Nebraska Center for Materials and Nanoscience, University of Nebraska, Lincoln, Nebraska 68588-0299, United States;* orcid.org/0000-0002-9952-9435; Email: tula.paudel@gmail.com

Author

Evgeny Y. Tsymbal − *Department of Physics and Astronomy & Nebraska Center for Materials and Nanoscience, University of Nebraska, Lincoln, Nebraska 68588-0299, United States;* orcid.org/0000-0002-6728-5480

Complete contact information is available at: https://pubs.acs.org/10.1021/acsomega.0c01139

Notes

The authors declare no competing financial interest.

■ ACKNOWLEDGMENTS

This work was supported by the Nebraska Public Power District through the Nebraska Center for Energy Sciences Research at the University of Nebraska-Lincoln, NCESR grant number 19-SE-2018. Computations were performed at the University of Nebraska Holland Computing Center. The atomic structure was produced using VESTA software.[27]

■ REFERENCES

(1) Shenoy, U. S.; Bhat, D. K. Bi and Zn Co-Doped SnTe Thermoelectrics: Interplay of Resonance Levels and Heavy Hole Band Dominance Leading to Enhanced Performance and a Record High Room Temperature ZT. *J. Mater. Chem. C* **2020**, *8*, 2036−2042.

(2) Bhat, D. K.; Shenoy, U. S. Enhanced Thermoelectric Performance of Bulk Tin Telluride: Synergistic Effect of Calcium and Indium Co-Doping. *Mater. Today Phys.* **2018**, *4*, 12−18.

(3) Bhat, D. K.; Shenoy, U. S. High Thermoelectric Performance of Co-Doped Tin Telluride Due to Synergistic Effect of Magnesium and Indium. *J. Phys. Chem. C* **2017**, *121*, 7123−7130.

(4) Shenoy, S.; Bhat, D. K. Enhanced Bulk Thermoelectric Performance of Pb 0.6 Sn 0.4 Te: Effect of Magnesium Doping. *J. Phys. Chem. C* **2017**, *121*, 20696−20703.

(5) Snyder, G. J.; Toberer, E. S. Complex Thermoelectric Materials. *Nat. Mater.* **2008**, *7*, 105−114.

(6) Shi, X.; Chen, L.; Uher, C. Recent Advances in High-Performance Bulk Thermoelectric Materials. *Int. Mater. Rev.* **2016**, *61*, 379−415.

(7) Bhat, D. K.; Shenoy, U. S. Zn: A Versatile Resonant Dopant for SnTe Thermoelectrics. *Mater. Today Phys.* **2019**, *11*, No. 100158.

(8) Huster, J. Crystal Structure of BaTiS3. *Z. Naturforsch.* **1980**, *35*, 775.

(9) Niu, S.; Joe, G.; Zhao, H.; Zhou, Y.; Orvis, T.; Huyan, H.; Salman, J.; Mahalingam, K.; Urwin, B.; Wu, J.; Liu, Y.; Tiwald, T. E.; Cronin, S. B.; Howe, B. M.; Mecklenburg, M.; Haiges, R.; Singh, D. J.; Wang, H.; Kats, M. A.; Ravichandran, J. Giant Optical Anisotropy in a Quasi-One-Dimensional Crystal. *Nat. Photonics* **2018**, *12*, 392−396.

(10) Sun, B.; Shulumba, N.; Niu, S.; Ravichandran, J.; Minnich, A. In *Ultralow Thermal Conductivity of Single Crystalline BaTiS3*, APS March Meeting; 2018; p S08.015.

(11) Bardeen, J.; Shockley, W. Deformation Potentials and Mobilities in Non-Polar Crystals. *Phys. Rev.* **1950**, *80*, 72−80.

(12) Dai, J.; Zeng, X. C. Titanium Trisulfide Monolayer: Theoretical Prediction of a New Direct-Gap Semiconductor with High and Anisotropic Carrier Mobility. *Angew. Chem., Int. Ed.* **2015**, *54*, 7572−7576.

(13) Togo, A.; Chaput, L.; Tanaka, I. Distributions of Phonon Lifetimes in Brillouin Zones. *Phys. Rev. B* **2015**, *91*, No. 094306.

(14) García-Fernández, P.; Verissimo-Alves, M.; Bilc, D. I.; Ghosez, P.; Junquera, J. First-Principles Modeling of the Thermoelectric Properties of SrTiO 3/SrRuO 3 Superlattices. *Phys. Rev. B: Condens. Matter Mater. Phys.* **2012**, *86*, 1−8.

(15) Niu, S.; Milam-Guerrero, J.; Zhou, Y.; Ye, K.; Zhao, B.; Melot, B. C.; Ravichandran, J. Thermal Stability Study of Transition Metal Perovskite Sulfides. *J. Mater. Res.* **2018**, *33*, 4135−4143.
(16) Sun, J.; Singh, D. J. Thermoelectric Properties of n -Type SrTiO 3. *APL Mater.* **2016**, *4*, No. 104803.
(17) Lee, S.; Kang, S. H.; Kwon, Y. K. Low Lattice Thermal Conductivity of a Two-Dimensional Phosphorene Oxide. *Sci. Rep.* **2019**, *9*, No. 5149.
(18) Blöchl, P. E. Projector Augmented-Wave Method. *Phys. Rev. B* **1994**, *50*, 17953−17979.
(19) Perdew, J. P.; Burke, K.; Ernzerhof, M. Generalized Gradient Approximation Made Simple. *Phys. Rev. Lett.* **1996**, *77*, 3865−3868.
(20) Kresse, G.; Furthmüller, J. Efficient Iterative Schemes for Ab Initio Total-Energy Calculations Using a Plane-Wave Basis Set. *Phys. Rev. B: Condens. Matter Mater. Phys.* **1996**, *54*, 11169−11186.
(21) Kresse, G.; Joubert, D. From Ultrasoft Pseudopotentials to the Projector Augmented-Wave Method. *Phys. Rev. B: Condens. Matter Mater. Phys.* **1999**, *59*, 1758−1775.
(22) Dudarev, S. L.; Botton, G. A.; Savrasov, S. Y.; Humphreys, C. J.; Sutton, A. P. Electron-Energy-Loss Spectra and the Structural Stability of Nickel Oxide: An LSDA+U Study. *Phys. Rev. B: Condens. Matter Mater. Phys.* **1998**, *57*, 1505−1509.
(23) Grimme, S.; Antony, J.; Ehrlich, S.; Krieg, H. A Consistent and Accurate Ab Initio Parametrization of Density Functional Dispersion Correction (DFT-D) for the 94 Elements H-Pu. *J. Chem. Phys.* **2010**, *132*, No. 154104.
(24) Madsen, G. K. H.; Singh, D. J. BoltzTraP, A Code for Calculating Band-Structure Dependent Quantities. *Comput. Phys. Commun.* **2006**, *175*, 67−71.
(25) Baroni, S.; Resta, R. Ab Initio Calculation of the Macroscopic Dielectric Constant in Silicon. *Phys. Rev. B* **1986**, *33*, 7017−7021.
(26) Chaput, L. Direct Solution to the Linearized Phonon Boltzmann Equation. *Phys. Rev. Lett.* **2013**, *110*, No. 265506.
(27) Momma, K.; Izumi, F. VESTA 3 for Three-Dimensional Visualization of Crystal, Volumetric and Morphology Data. *J. Appl. Crystallogr.* **2011**, *44*, 1272−1276.

https://dx.doi.org/10.1021/acsomega.0c01139
ACS Omega 2020, 5, 12385−12390